The Energy Spectrum of Cosmic-Ray Electrons from 10 to 100 GeV Observed with a Highly Granulated Imaging Calorimeter

2001 ApJ 559 973

(http://iopscience.iop.org/0004-637X/559/2/973)

THE ASTROPHYSICAL JOURNAL, 559:973–984, 2001 October 1

THE ENERGY SPECTRUM OF COSMIC-RAY ELECTRONS FROM 10 TO 100 GeV OBSERVED WITH A HIGHLY GRANULATED IMAGING CALORIMETER

S. TORII, T. TAMURA, AND N. TATEYAMA
Institute of Physics, Kanagawa University, Rokkakubashi, Kanagawa-ku, Yokohama 3-27-1, Japan; torii@phu2.b6.kanagawa-u.ac.jp
K. YOSHIDA
Department of Industrial Engineering and Management, Kanagawa University, Yokohama, Japan
J. NISHIMURA AND T. YAMAGAMI
Institute of Space and Astronautical Science, Sagamihara, Kanagawa, Japan
H. MURAKAMI
Department of Physics, Rikkyou University, Tokyo, Japan
T. KOBAYASHI
Department of Physics, Aoyamagakuin University, Tokyo, Japan
Y. KOMORI
Kanagawa Prefectural College, Yokohama, Kanagawa, Japan
K. KASAHARA
Department of System Engineerings, Shibaura Institute of Technology, Omiya, Saitama, Japan
AND
T. YUDA
Solar-Terrestrial Environment Laboratory, Nagoya University, Nagoya, Aichi, Japan
Received 2000 September 17; accepted 2001 May 9

ABSTRACT

Cosmic-ray electrons[1] have been observed in the energy range from 12 to ~100 GeV with a new balloon-borne payload, the Balloon-borne Electron Telescope with Scintillating Fibers (BETS). This is the first publication of the absolute energy spectrum of electrons measured with a highly granulated fiber calorimeter. The calorimeter makes it possible to select electrons against the background protons by detailed observation of both the longitudinal and the lateral shower development. The performance of the detector was calibrated by the CERN-SPS accelerator beams: electrons from 5 to 100 GeV, protons from 60 to 250 GeV. The balloon observations were carried out twice, in 1997 and 1998, at the Sanriku Balloon Center (Institute of Space and Astronautical Science) in Japan. The observation time was ~13 hr in all at an altitude above 34 km. A total of 1349 electron candidates were collected, and the 628 events with energies above 12.5 GeV, well above the geomagnetic rigidity cutoff of ~10 GV, have been used to compose a differential absolute energy spectrum at the top of the atmosphere. The energy spectrum is described by a power-law index of 3.00 ± 0.09, and the absolute differential intensity at 10 GeV is 0.199 ± 0.015 m^{-2} s^{-1} sr^{-1} GeV^{-1}. The overall shape of the energy spectrum in 10 ~ 100 GeV can be explained by a diffusion model, in which we assume an energy-dependent diffusion coefficient ($\propto E^{0.3}$) for an injection spectrum, $E^{-2.4}$.

Subject headings: balloons — cosmic rays — diffusion — supernovae: general

1. INTRODUCTION

The major goals in cosmic-ray studies are to make clear the origin, the acceleration mechanism, and the propagation properties inside the Galaxy. Along this line, many efforts have been expended to observe a precise spectrum of the various components in cosmic rays. Electrons in cosmic rays have unique features compared with other components since they are related directly to a number of significant astrophysical questions, such as the nature and distribution of the sources in the Galaxy and the characteristics of cosmic-ray propagation in the Galactic disk and halo.

From radio observations, it is known that supernova remnants (SNRs) are the most likely source of negative electrons. It was recently predicated that one shell-type supernova (SN 1006) is a candidate electron source to around 100 TeV from the observations of nonthermal X-rays by the *ASCA* satellite (Koyama et al. 1995) and TeV gamma rays by the CANGAROO group (Tanimori et al. 1998). The total energy output (>1 GeV) from SN 1006 was estimated at ~10^{48} ergs. This can explain the energy budget of cosmic-ray electrons, assuming each supernova accelerates similar amounts of electrons at an explosion rate of once per ~30 yr.

During propagation through the Galaxy from the sources, high-energy electrons lose their energy rapidly by synchrotron radiation in the Galactic magnetic field and the inverse Compton process on the interstellar photon field. The energy-loss rate is proportional to the square of the energy; the lifetime becomes shorter in proportion to the inverse of energy. This also brings a steepening of the observed spectrum; the spectral index at low energy, γ, may increase to a maximum value, $\gamma + 1$. In the intermediate energy region, the change of spectral index is given by the

[1] We shall not distinguish electrons from positrons in this paper; the term "electrons" is used for the sum of particles regardless of charge. When we must identify the charge, we will use the terms " negative electrons" or "positrons."

propagation characteristics, the size of the Galactic halo and disk, the distribution of sources, the reacceleration in interstellar space, etc.

Theoretical studies including these effects were done to interpret the electron propagation process—diffusion model and leaky box model—in the Galaxy (Nishimura et al. 1980; Protheroe 1982; Berezinskii et al. 1990). The electron flux has been calculated to investigate the local source effects (Atoyan et al. 1995; Nishimura et al. 1997), the relation to the Galactic diffuse gamma rays (Pohl & Esposito 1998), and also the relation to other cosmic-ray components (Moskalenko & Strong 1998). From these calculations, many important theoretical aspects have been derived for the energy spectrum. However, the observed spectrum still could not meet the requirements of accuracy to define the parameters. The reason the electron measurements still cannot have sufficient accuracy, despite so many observations during the last ~ 30 yr, is mainly because of their low intensity ($\sim 1\%$ of protons), which requires, in particular at high energies, rather large (and heavy) detectors with the capability of effective discrimination against the proton-induced background.

Many novel detectors have been invented to overcome the difficulty by using a combination of an electromagnetic calorimeter and a device for particle identification, such as a gas Cherenkov counter (Müller & Meyer 1973), a transition radiation detector (Prince 1979; Tang 1984; Müller & Tang 1987), or a magnet spectrometer (Buffington, Orth, & Smoot 1975; Golden et al. 1984, 1994). Recent advanced detectors for measuring positrons separately from negative electrons have been constructed in combination with a transition radiation detector (Barwick et al. 1997) or a Ring Imaging Cherenkov (RICH) detector (Boezio et al. 2000) with a system of magnet spectrometer and calorimeter. Since the positron flux is expected to be lower by one order than the negative electron at the energies of interest, these have accomplished a proton rejection power of $\sim 10^5$. These were proven to be successful for measuring the positrons and the negative electrons to ~ 50 GeV with very low background.

The pioneering work using emulsions to detect high-energy electrons was first done by the Tata group (Daniel & Stephens 1965). They used emulsion stacks and detected electrons up to several hundred GeV. The merit of the emulsion detector results from the separation of electron-induced showers from those of hadron origin by inspection at the starting point. An emulsion chamber (ECC) developed for more effective observations has been measuring the electrons uniquely in the TeV region through its excellent capability of electron identification and the large acceptance (Nishimura et al. 1980). The exposure factor of ECC has attained 7.7 m^2 day sr, which is larger than the other observations by nearly 2 orders of magnitude. The group already has achieved extension of the observed spectrum to a few TeV (Kobayashi et al. 1999).

ECC is not, however, easily capable of detecting electrons below a few 100 GeV because event detection by naked-eye scanning is not available at such lower energies given the accumulation of background tracks. One needs the microscope scanning below 100 GeV, and the exposure factor is less than 0.1% of that in the TeV region. The observation of electrons from 10 to several 100 GeV is still far from the completion necessary for detailed discussion of the acceleration and propagation of the electrons.

The Balloon-borne Electron Telescope with Scintillating Fibers (BETS) has been developed as a detector that preserves the superior qualities of both electronic detectors and emulsion chambers. Namely, it can observe the details of shower starting points and shower development with a timing capability for the background rejection. The high-energy showers of electrons are frequently accompanied by the backward scattering particles, which might introduce an inevitable confusion in the identification of incident particles. To remedy this problem, we employed the scintillating-fiber layers in BETS for a sufficient tracking capability. Our primary aim for the new measurements with the BETS is to determine the energy spectrum of electrons in the energy region between 10 and 100 GeV by applying the latest technology for electron identification, which is being used for the first time.

To achieve the largest acceptance within the limits of balloon observation, we have adopted an imaging calorimeter using no additional equipment to identify the sign of charge. Therefore, we did not separate positrons among electrons. The positron flux has been measured to be less than several percent of the negative electrons around 10 GeV, and a primary source of positrons is quite unlikely (Barwick et al. 1998; Boezio et al. 2000). The positrons at higher energies must be quite scanty ($\sim$ a few percent of negative electrons), as estimated by the calculations (Protheroe 1982; Moskalenko & Strong 1998).

In the following, we shall present our first results on the absolute differential energy spectrum of electrons in the $12 \sim 100$ GeV range at the top of the atmosphere, observed by the two flights in 1997 and 1998 for 12.8 hr in total at the Sanriku Balloon Center in Japan. We also describe the instrumentation, the calibration of the detector at accelerator beams, and the analysis method of flight events. Finally, we discuss the results by comparing them with a diffusion-model calculation.

2. INSTRUMENTATION

Aiming at the measurements of electrons above 10 GeV, we have developed a new type of imaging calorimeter. The required capability, high discrimination power against the proton background and large acceptance, was accomplished in the detector through the high granulation in shower imaging for detailed observation both of the longitudinal and lateral shower development. Because of the excellent tracking capability of shower particles, it can have an additional proton-rejection power compared with the usual calorimeter observing only the longitudinal shower development. The BETS has a rejection power considerably better than 10^3 and a relatively large acceptance (~ 320 cm^2 sr) because of the simple structure.

The detector was extensively calibrated at the accelerator beams of the Super Proton Synchrotron (SPS) of CERN (Tamura et al. 2000), and the performance was investigated by full Monte Carlo (MC) simulations using the EPICS code developed by one of the authors (K. K.).[2] Reliability of the simulation code has been tested already by comparing the calculation results with those of accelerator experiments with several types of detectors.

[2] Information on the EPICS code, including comparison with other major codes familiar in high-energy physics, GEANT, and so on, is available at http://eweb.b6.kanagawa-u.ac.jp/~kasahara/.

A general description of the entire system of the BETS is presented elsewhere (Torii et al. 2000a). Here, we describe the part of the apparatus relating to the data analysis.

2.1. *Imaging Calorimeter*

The calorimeter consists of eight lead plates, each 5 mm (0.9 radiation length) thick, nine belts of scintillating fibers and three plastic scintillators, each 10 mm thick. The plastic scintillators were adopted for the instrument trigger and the energy measurement, and the scintillating optical fibers were used for observing the shower particles developing in lead with an image-intensified CCD camera. The design, presented schematically in Figure 1, has been extensively studied by MC simulations to accomplish the best performance both in the electron selection and the energy measurement.

The scintillating optical fiber, Kuraray SCSF77, has a one millimeter diameter and is composed of a poly-styrene core ($n = 1.59$) surrounded by a poly-methylmetacrylate (PMMA) clad ($n = 1.49$). These 280 fibers form a layer with a one millimeter pitch. In each belt, two layers were set in right angle with each other to observe the projected shower profile in x- and y-directions. The effective area covered by these orthogonal layers was nearly 28×28 cm^2. In the converter part shown in Figure 1, there were three fiber belts, each with $4x$ and $4y$ layers. These ensure the detection of minimum ionizing particles (MIP) incident on the top of the detector. The starting point of the shower was determined with an accuracy of 0.9 radiation lengths. Detection efficiency of MIP in the four-layer belt was 98% with the requirement that more than two of the layers have signals. There were six belts in the calorimeter part: one layer in each direction. The total number of layers was 36 (18 in each of two orthogonal views, x and y); the total number of scintillating fibers was 10,080.

For the readout of scintillation light in the fibers, we used an image-intensified CCD camera in each direction of x and y. The input window of each camera had the shape of a circle of 10 cm diameter. Since the fiber belt had a width of 28 cm, it was not possible to contact the edge of the fiber belt to the input window without a light guide to reduce the width of the belt. Each fiber was, therefore, spliced one by one to a clear fiber as a light guide at the detector edge. The clear fibers were chosen to avoid noise signals from the light guide since they have no efficiency for charged particles. For the adjustment of size to the camera window, the clear-fiber layer was equally divided by four into 70 mm widths and piled up to make a tab of fibers as shown in Figure 2. The 72 (i.e., 4×18) clear-fiber groups in one direction and the five extra tabs of clear fibers that were attached to the light-emitting diode (LED) in the opposite side are stacked and held together in a rectangular block with a cross section of nearly 70×70 mm^2. The LED was irradiated during

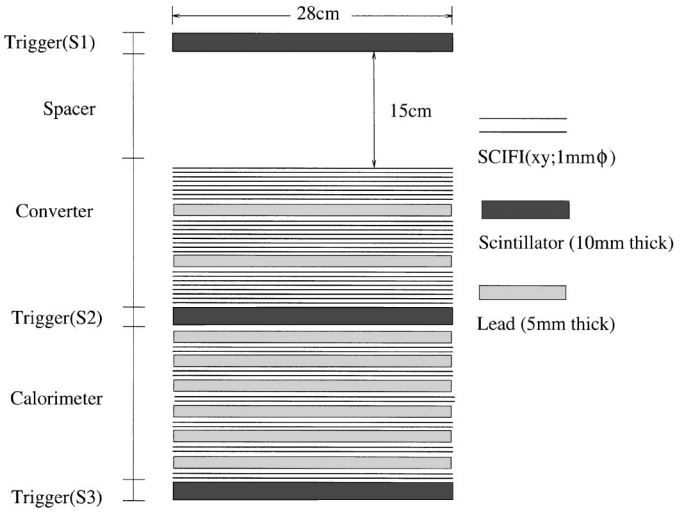

FIG. 1.—Schematic side view of the imaging calorimeter. Vertical dimension of the calorimeter is not exactly scaled to show the details of structure. The height is nearly 28 cm including the spacer. The total thickness of the calorimeter is 7.3 radiation lengths and 0.32 nuclear interaction lengths, taking into account all the material. During the flights, the calorimeter was covered by a vessel to shade light and keep the inside pressure.

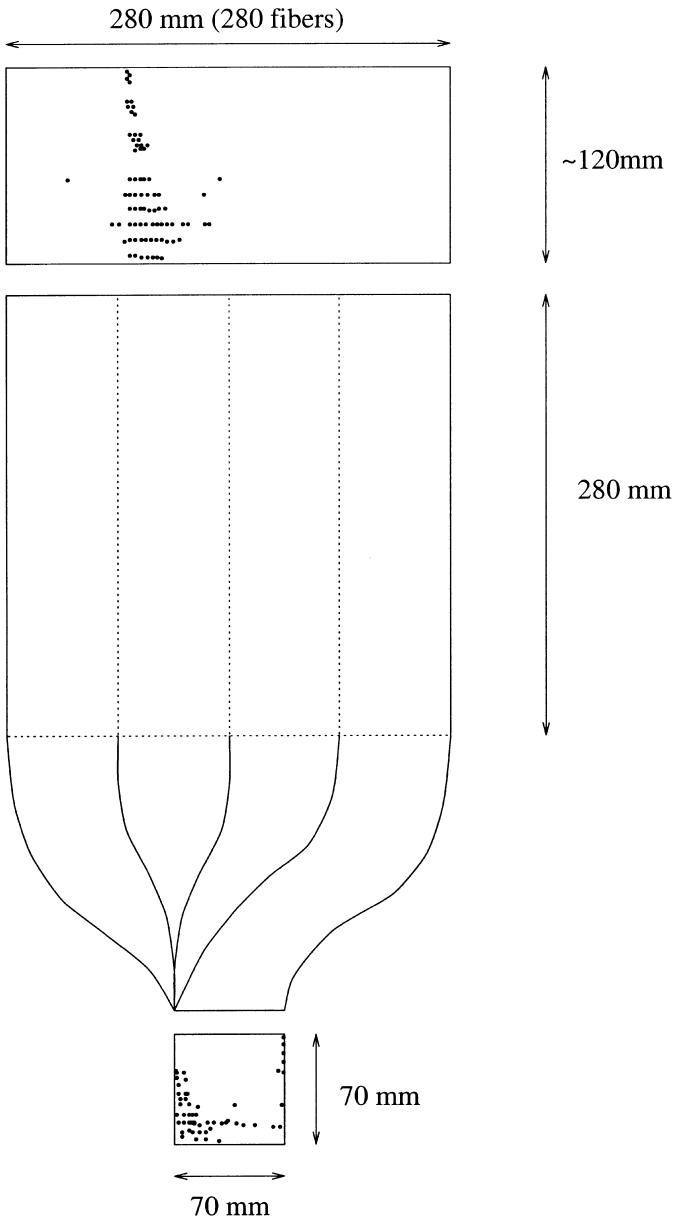

FIG. 2.—Conceptual top view of one scintillating fiber belt (*middle*) and the side view of an illustrated shower image observed at the fiber outputs (*top*) and at the inputs of the CCD camera (*bottom*). There are 18 fiber layers with a width of 280 mm at the detector and 72 layers with a width of 70 mm at the readouts. The illustrations show how the shower image at the detector is transformed on the CCD image.

the experiment for alignment check of the fiber system and sensitivity test of the camera.

2.2. *Instrument Trigger*

The instrument trigger was executed by threefold coincidence of signals from the plastic scintillators placed at each depth in the calorimeter, S_1, S_2 and S_3. Each scintillator was viewed through a light guide by a 2 inch diameter photomultiplier tube. The anode signal was employed to make the instrument trigger signal; the dynode signal was used to measure the energy deposition. The dynode signal was digitized with a 12-bit analog-to-digital converter (ADC) after preamplification and shaping.

By the optimization using simulation calculations, the discrimination levels in each scintillator were set to $0.7 \sim 5$ at S_1, ≥ 10 at S_2, and ≥ 40 at S_3 (in units of a minimum ionizing particle), respectively. These criteria require a penetrating particle that deposits energy larger than a 10 GeV electron in the calorimeter. We could exclude most protons and heliums that have no interaction and a considerable portion of those that have interactions, especially at a depth below the converter part. The heavier particles were not triggered since they have an energy loss larger than five particles at S_1. The highest proton-rejection power of ~ 100 at 85% electron efficiency could be expected above 10 GeV by the simulations described in § 3.2.

2.3. *Image-intensified CCD Camera*

The image-intensified CCD camera system was developed by improving a commercial product, Hamamatsu II-100. It consists of an image intensifier followed by two-stage image intensifiers with a microchannel plate (MCP) and a CCD camera connected via taper-fiber optics. The first-stage image intensifier is composed of an input window of 10 cm diameter, photocathode, focusing electrodes, and phosphor screen target. The input window is a fiber optical plate, and the photocathode is made of bialkali, which matches with the spectrum of the scintillation light. It fulfills the function as a light amplifier and an image reducer to the following image intensifier with a one-inch diameter window. The amplification process is repeated in the later two-stage image intensifiers, which have multialkali photocathodes matching the spectrum of the emission light of the phosphor screen. The last-stage image intensifier has a gate function by giving the inverse voltage to the MCP while waiting for a trigger timing. The width of the timing gate was optimized at 7 μs to get enough photons while avoiding the effects of overlapping of the preceding and following events. Although the highest gain of photon amplification exceeds 10^6, the gain was adjusted to a lower level to get the largest dynamic range by reducing the saturation effects in the CCD camera.

We used a commercial product CCD camera (SONY XC77RR-CE), which has 756(H) $\times$ 581(V) pixels with a cell size of 11(H) $\times$ 11(V) μm. The real size of clear fiber outputs (70 $\times$ 70 mm) is covered within an area of 512 $\times$ 512 pixels (5.6 $\times$ 5.6 mm) on the sensitive area of CCD. The CCD camera has a shutter function with a gate width of 1/1360 seconds delayed by 1 μs from the external trigger signal.

A VME-oriented video module was developed especially for the experiment. It has a function to read 512 $\times$ 256 pixels made by the 2:1 interlace CCD scanning method. The signals were digitized with an eight-bit flash ADC. An image of 256 $\times$ 256 "picture elements" was used for each event by averaging the two signals in horizontally neighboring pixels.

3. ANALYSIS OF IMAGE DATA AND PROTON REJECTION

3.1. *Reconstruction of Shower Image*

The shower image observed in coordinates of the CCD picture elements should be transformed to the fiber positions in detector space. For this purpose, it was necessary to define the positions of each fiber on the CCD image. The positions of all fibers were allocated by observing cosmic-muon tracks on the ground level. When a muon passes over one scintillating fiber, the photons emitted in the fiber make a bright spot (cluster of pixels) on the CCD image. In Figure 3, we present a two-dimensional scatter plot of the centroids of the spot, which were obtained by superimposition of many events ($>10^6$) of muon tracks. The centroids distribute within a cross section of fiber (a circle of 1 mm diameter), and the shapes of each cross section were clearly resolved with each other.

The center of each fiber was determined within an accuracy of one pixel by the two-dimensional Gaussian fit to the distribution of the centroids, as is also presented in Figure 3. Then, the complete map of 5040 fibers was applied for the reconstruction of the shower image in detector space. Relative displacement of the whole position was calibrated by the LED in each experiment, although it did not usually exceed one picture element.

Examples of the reconstructed shower image and the raw CCD image observed in flight are presented in Figure 4. The signal intensity in one fiber was calculated by summing the CCD signals in the fiber position. The dashed line in the reconstructed image displays the shower axis obtained by an energy-weighted least-square fitting. A typical event, which shows development of an electron-induced shower, as presented in the upper panel of the figure, always has a concentrated structure of shower particles along the axis. On the contrary, that of proton-induced shower usually has secondary tracks, as in the lower panel of the figure, and presents a wider lateral spread. This difference in lateral shower development could serve as another capability of proton discrimination as described below.

3.2. *Proton Rejection by Simulation*

Average lateral spread of an electromagnetic shower in lead is roughly estimated at ~ 1.6 cm (one Moliere unit). However, a proton-induced shower should have a wider spread because of the spread of secondary pions in the nuclear interactions. This difference was clearly observed in the real images. The method for electron selection by the imaging analysis was developed by an analysis of the simulated events that fulfill the criteria of the "instrument trigger." In the simulation, we assumed a differential energy spectrum of protons ($\propto E^{-2.7}$) and of electrons ($\propto E^{-3.0}$). The flux ratio of electrons to protons was nominally taken as 1:150 above 10 GeV. These particles were sampled to be incident uniformly in positions on the top of the detector and isotropically in arrival directions.

For the simulated events of electrons and protons, we produced distribution of the ratios (RE) of energy deposition within 5 mm from the shower axis to the total, as presented in Figure 5. The distribution of the electrons is seen to be separated from that of the protons in the region of higher energy concentration. The ratio of proton events

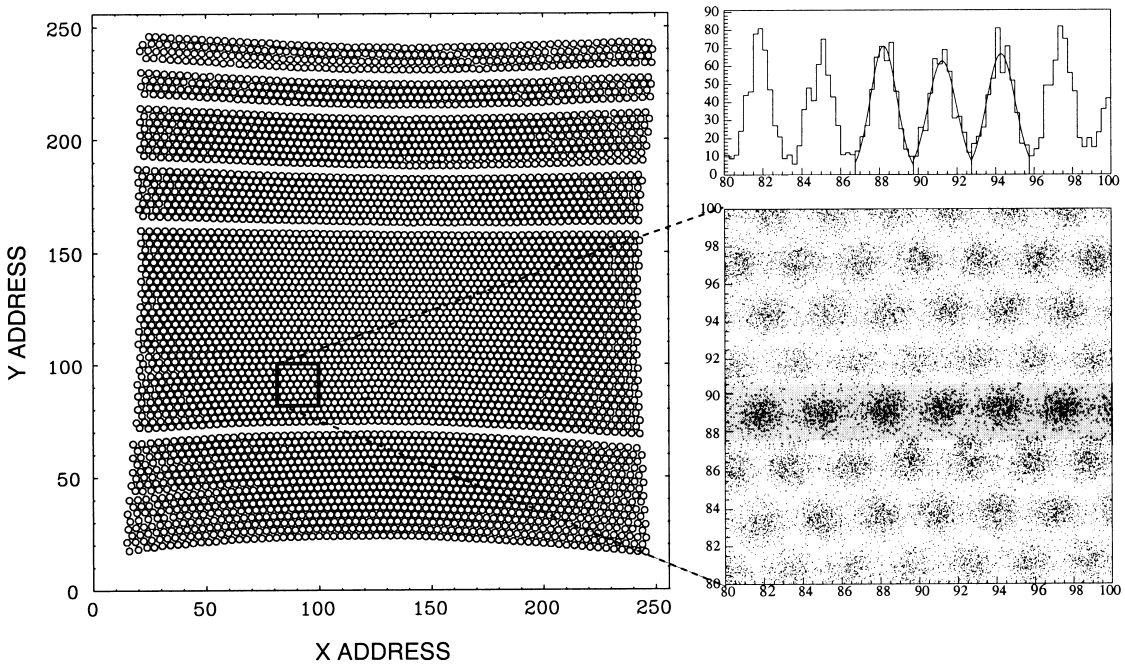

FIG. 3.—Allocation map of 5040 fibers on the CCD image (*left*) and two-dimensional scatter plot of centroids of the spotlike CCD image by cosmic-ray muons (*right*). A circle in the map corresponds to the cross section of one fiber. The center of circles was obtained by a two-dimensional Gaussian fit of the centroids as presented at the upper right.

in the region of $RE \geq 0.7$ is $\sim 5\%$, while 85% of the electron events are in the region. Therefore, the electron fraction is enhanced by ~ 20 times in the events with $RE \geq 0.7$. The total rejection power is expected to be ~ 2000 since 99% of protons have already been rejected by the "instrument trigger."

4. DETECTOR CALIBRATIONS AT ACCELERATOR BEAMS

For the calibration of the detector, we carried out an extensive beam test of electrons in 1996 and of protons in 1997. The energies range from 5 to 100 GeV for electrons and from 60 to 250 GeV for protons. The energy resolution, the angular response, and the detection efficiency were calibrated for electrons. The proton-rejection capability was examined at various conditions of beam energies, incident positions on the detector, and incident angles. The detector was irradiated in the beams under exactly the same conditions as the balloon experiment to estimate the real performance. In Table 1, we summarize the performance of the detector, which should be proven in this section.

4.1. *Energy Resolution*

The energy of electromagnetic shower was measured by the pulse height at the bottom scintillator, S_3. As presented

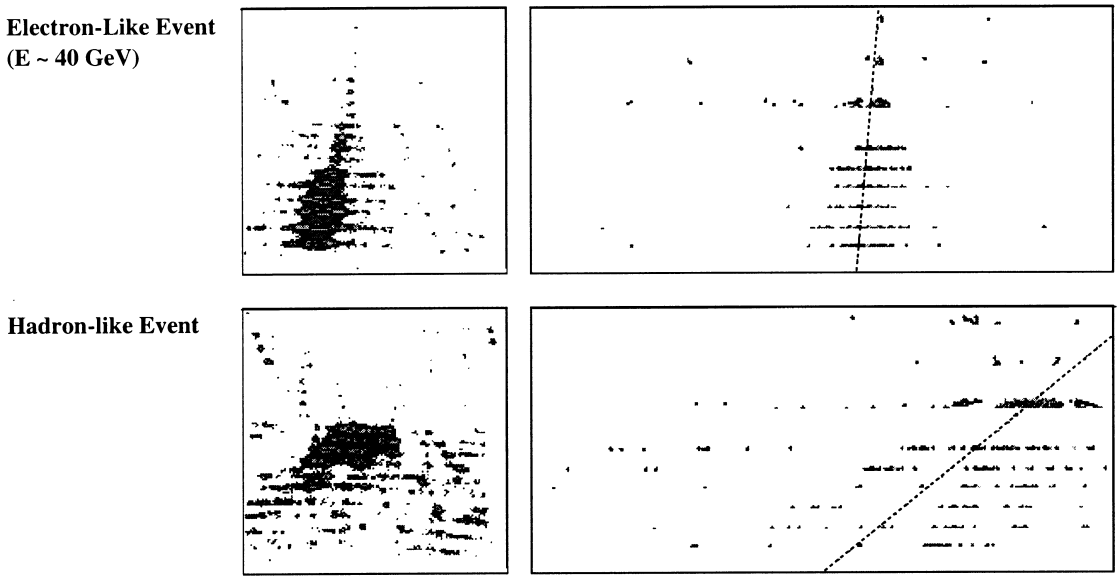

FIG. 4.—Examples of raw CCD images of an observed shower (*left*) and the reconstructed image in detector space (*right*). The intensities in both images are presented by an eight-bit gray scale. The upper image is of a typical electron-induced shower and the lower is of a proton-induced one. The real size is 5.6 × 5.6 mm for the CCD image and 28 × 12 cm for the reconstructed image.

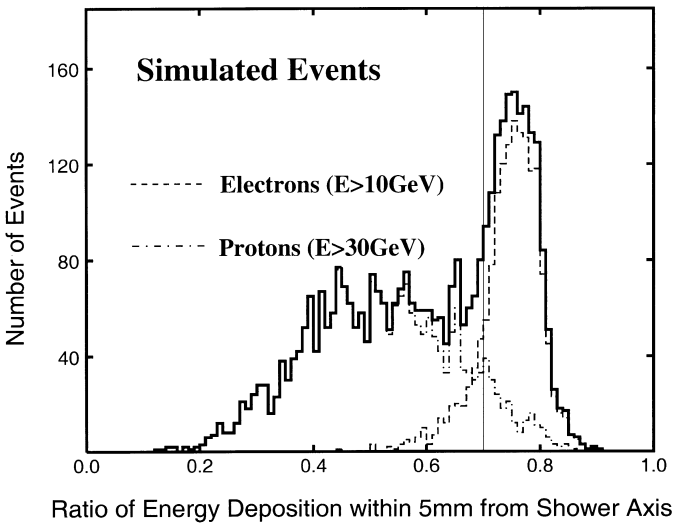

FIG. 5.—Distribution of *REs* for the simulated proton and electron events after the "instrument trigger" (see text).

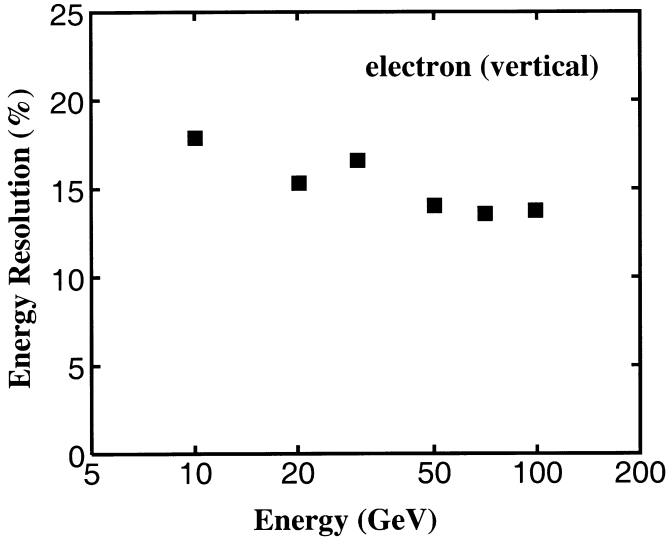

FIG. 7.—Energy dependence of the energy resolutions for electrons. The incident direction is vertical. The errors are less than the size of the symbol.

in Figure 6, the relation between the average of pulse heights and the electron energies is almost linear since the depth of S_3 is near the shower maximum at these energies. The energy resolution was obtained by using a Gaussian fit to the pulse height distribution at each energy. Figure 7 shows that the energy resolution is nearly constant, ranging from 14% to 17% in the energy region from 10 to 100 GeV.

TABLE 1

INSTRUMENT PERFORMANCE SUMMARY

Characteristics	Performance
Energy range	10 GeV ~ a few 100 GeV
Geometric factor ($\theta < 30°$)	~320 cm^2 sr
Proton/Electron discrimination	~2000
Energy resolution	14% ~ 17%
Angular response	0°.8 ~ 1°.3
Total weight	~320 kg
Power consumption	130 W

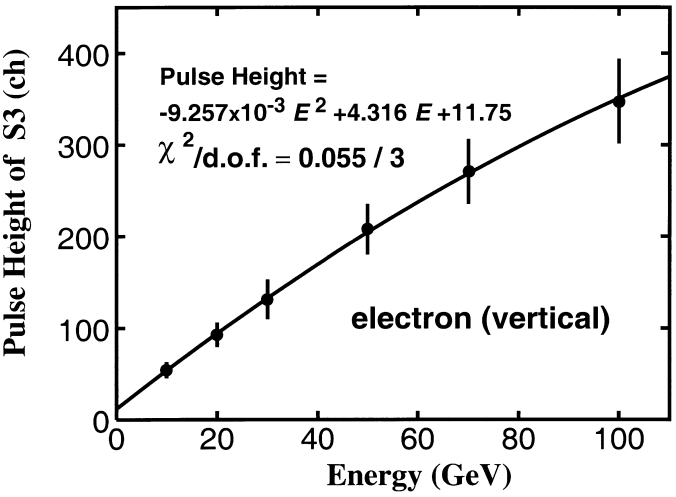

FIG. 6.—Relation of electron energies and pulse heights (in ADC count) in the bottom scintillator, S_3, observed with the CERN-SPS beams. The error bars are standard deviations obtained by a Gaussian fit to the energy distribution.

Such a small change in the energy resolution has little effect on both the slope of the energy spectrum and the absolute flux from the measurements, as is shown later (§ 7.1).

4.2. *Angular Response*

The angular response of the electrons was investigated by calculating the opening angle between the fitted shower axis and the incident direction of the beam. We did not consider the spread of beam angles since it was negligible in comparison with the fitting accuracy. In Figure 8, we present the angular distributions at an incident angle of 15° for the electron beams. The distribution at each energy could be fit with a Gaussian function as shown by the solid curve in the figure. Systematic displacements in the average angle from 15° (given by the "mean" in the figure), were caused mainly by errors in the detector setting and not in the axis fittings.

The angular resolution becomes better with increasing energies, as is presented in Figure 9, from 1°.3 at 10 GeV to 0°.8 at 100 GeV. These resolutions were so good as to estimate accurately the shower axis in the image analysis of the flight events.

4.3. *Electron Trigger Efficiency*

The pulse height at the bottom scintillator, S_3, is critically important in the instrument trigger. The discrimination level, therefore, was carefully determined to be an optimum level (40 particles in simulation) by using the calibration data. Another important issue in the instrumental trigger was the effect of backscattered particles on the top scintillator, S_1. The reason we put the maximum level (five particles in simulation) at S_1 in the trigger criteria was to reject high-energy protons that produce the backscattered particles over five particles and heavier particles ($Z > 2$) that have an ionization loss exceeding the level. The trigger efficiency of heliums was considerably less than protons (~10%), even in the case in which they have nuclear interactions. On the other hand, the level must be optimized as low as possible not to miss the electrons with backscattered particles in higher energies.

Figure 10 presents a relation of the trigger efficiency of electrons and the number of particles observed at S_1 (N_1).

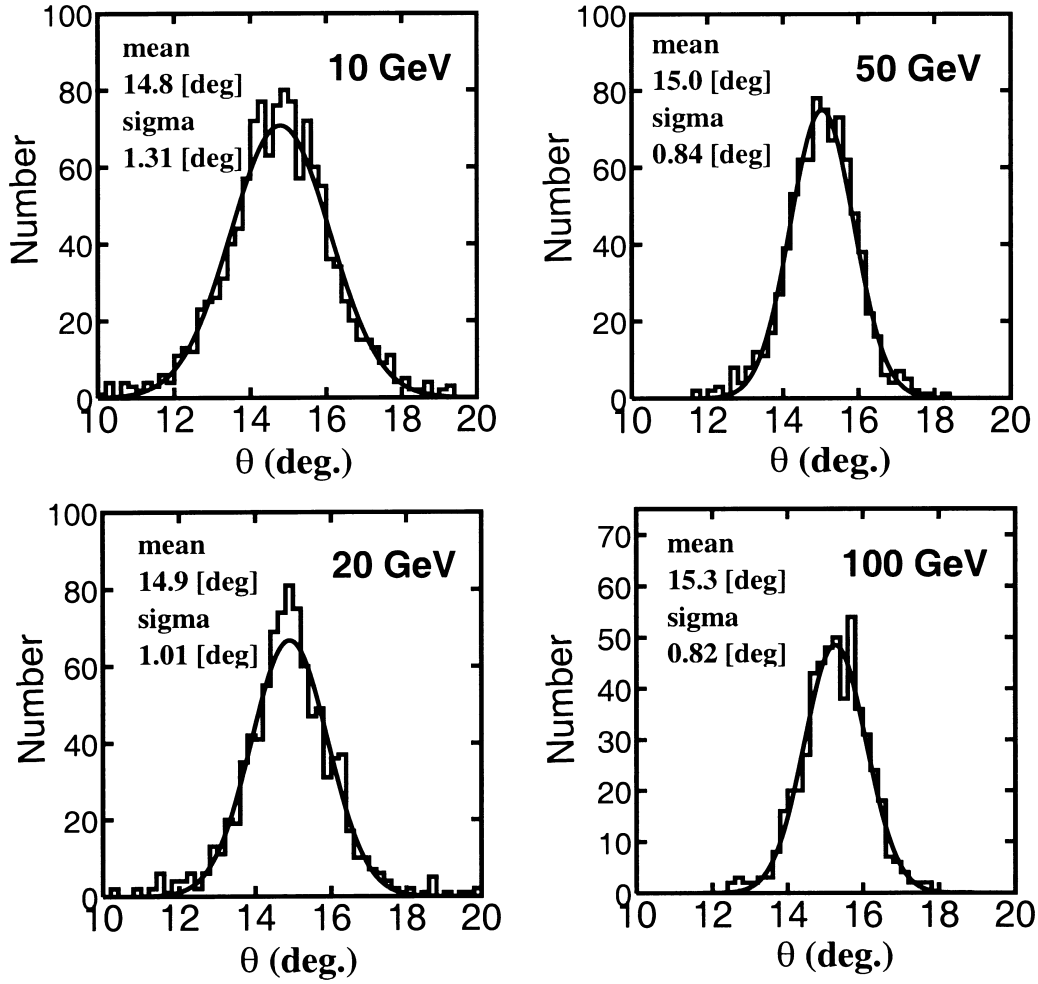

FIG. 8.—Angle response of the fitted shower axis to the beam direction for electrons at each energy level, observed with the CERN-SPS beams. The solid curve is a Gaussian distribution of the best fit to the data.

The efficiency depends on N_1 below three particles and is nearly 100% for $N_1 > 5$, irrespective of energies. Thus, we could conclude that the discrimination at S_1 ($0.7 \sim 5$ particles) was very effective to reject background particles while keeping the electron efficiency nearly complete. As with the above results, the event rejection on-board during flight was so efficient as to keep the live time of data acquisition better than ~80%.

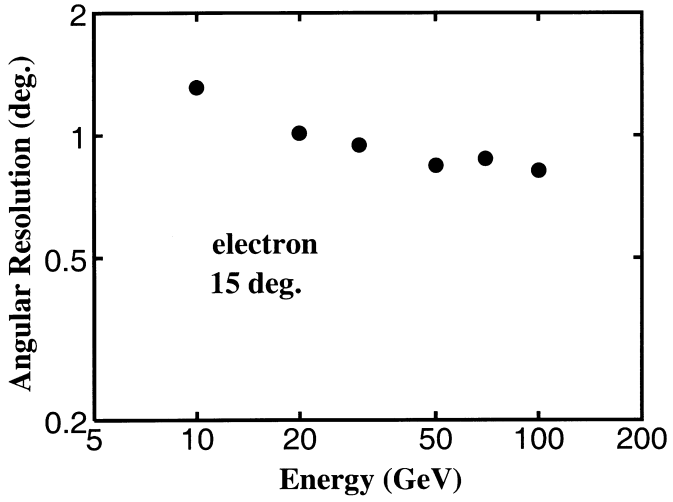

FIG. 9.—Energy dependence of the angular resolution. The errors are smaller than the size of the symbol.

4.4. *Electron and Proton Efficiency*

Simulation results on the electron selection using the energy concentration parameter *RE* were also examined by the accelerator beams. Figure 11 presents the *RE* distributions for electrons with an incident angle of 0° (*vertical line*) and 30°. The observed distributions have a clear peak around $RE \sim 0.8$, similar to the simulated events, and we applied the cut of events in $RE > 0.7$ (*RE*-cut) for electrons. The surviving probabilities with this cut were obtained for the different energies and incident angles as presented in Figure 12.

The probabilities for electrons in $10 \sim 50$ GeV are consistent with the simulation expectations and hardly depend on the incident angle. However, those at energies higher than 50 GeV decrease slightly with energy depending on the incident angle. This change was not expected from the simulations and could be caused by an instrument problem in which the CCD signals saturate in the shower core at higher energies.

The surviving probabilities of protons were also estimated by the *RE*-cut. These depend strongly on the incident angle; ~10% for the vertical and less than a few percent for those larger than 30°. The probability should be ~5%, which is consistent with simulation at the average of inci-

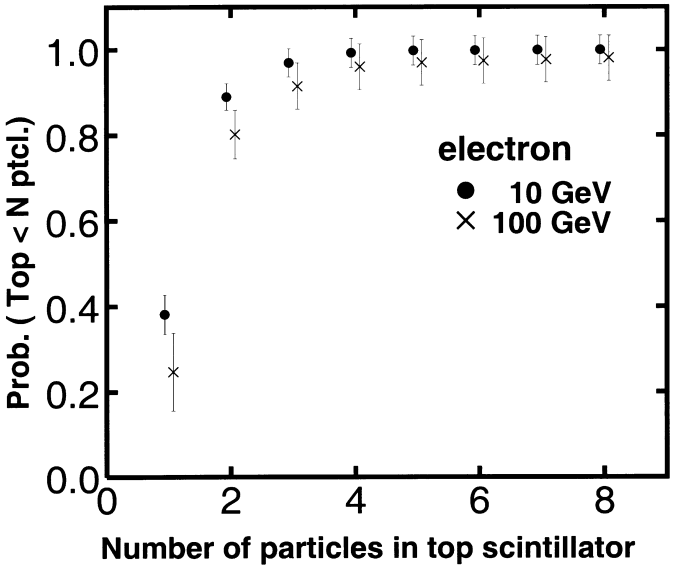

FIG. 10.—Trigger efficiency of electron-induced showers as a function of the number of particles at the top scintillator, S_1, from the CERN-SPS beams. Because of the backscattered particles from the shower, more than one particle is usually observed at S_1.

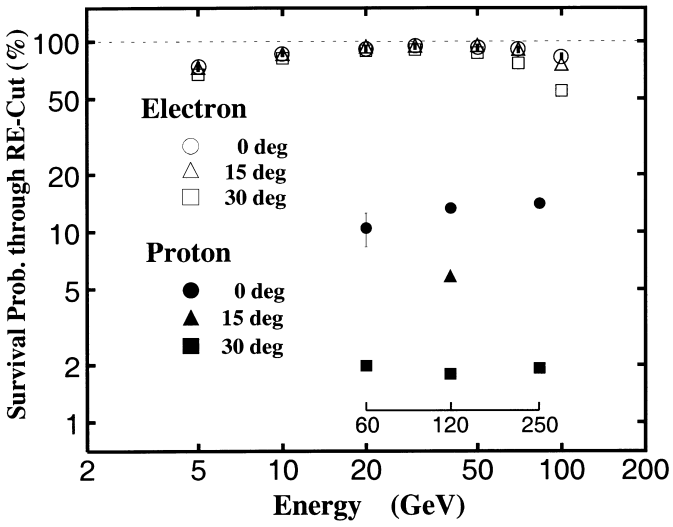

FIG. 12.—Surviving probability through the *RE*-cut for the electron-induced showers and the proton-induced ones observed with the CERN-SPS beams.

dent angles ($\sim 20°$) of the observed events. The average energy of the proton-induced showers in the triggered events was lower by nearly three times that of the electron-induced showers for the same incident energy. Therefore, the proton energy in the figure was scaled by three times compared to the electron energy.

5. BALLOON FLIGHT

The balloon flights were carried out two times at the Sanriku Balloon Center (39°.2 latitude north, 141°.8 longitude east) in Japan; the first, BETS97, on 1997 June 2, and the second, BETS98, on 1998 May 24–25. The geomagnetic rigidity cutoff is about 10 GV at the vertical. The data were collected for 4.5 hr at a level altitude of 35 ~ 36 km (35.7 km on average) in BETS97 and for 8.3 hr at a level of nearly 35 km in BETS98. The level altitude during observations was very stable both in BETS97 and BETS98, and the variation of attitudes was mostly within 0.5 km (~ 0.2 g cm^{-2} in residual atmosphere). The corrections caused by the residual atmosphere were done by using the average altitude in each flight.

The rate of instrument triggers at flight level was ~ 1.7 Hz in both flights, and the data size recorded on board was 0.7 Gbyte in BETS97 and 2.0 Gbyte in BETS98. The instrument was recovered from the sea without any damage, and the same detector was used for both flights.

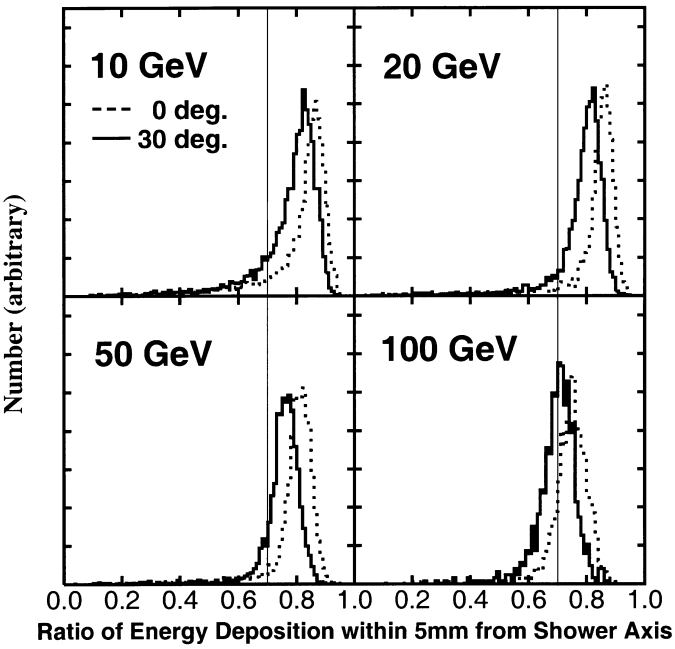

FIG. 11.—*RE* distribution of electron-induced showers observed with the CERN beams. Dotted lines present the distribution for showers with an incident angle of 0° (*vertical line*); solid lines for those with an incident angle of 30°.

6. DATA ANALYSIS

6.1. *Event Selection by Imaging Data*

Most of the backgrounds triggered during the flights were particles incident from the side of the detector. Therefore, the analysis of flight data was done, first of all, for the image reconstruction of all events by the procedures described in § 3.1. The event reduction for the electron selection was performed by the following cuts.

1. Axis selection: The shower axis passes through the top and bottom detector.
2. Angle cut: The zenith angle of the shower axis is less than 30°.
3. Charge selection: Charge of the incident particle is single.
4. Edge cut: The shower axis crosses the bottom scintillator in the region inside 20 mm from the edge.

Cuts 1 and 2 should select the "contained" events that enter from the top of the detector with a zenith angle less than 30°. The angle cut was applied to keep the proton rejection power higher as well as to reduce the effects of atmospheric electrons. The selection must be very reliable since the accuracy of reconstructed shower axis was as good

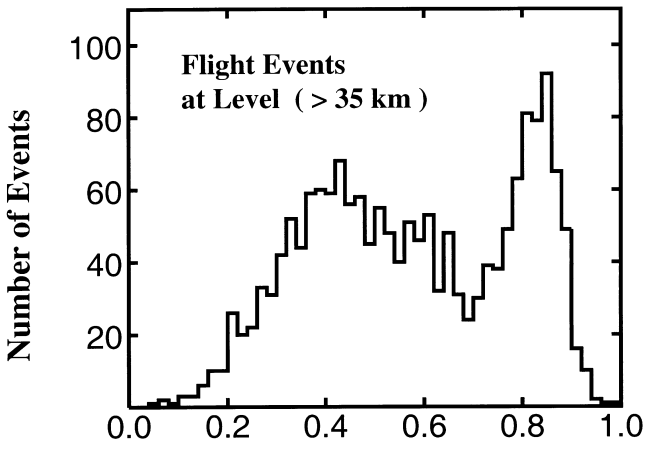

FIG. 13.—Observed *RE* distribution for the flight events at an altitude over 35 km in BETS97. The events plotted here have been selected by the criteria 1 to 3 in the text.

as $\sim 1°$. Only a few percent of the recorded events pass through these criteria.

Charge of the incident particle was estimated at the four-layered fiber belts in the converter part of calorimeter. The charge resolution by the scintillating fibers was examined by using the heavy-ion tracks observed in the test flight in 1995. For this purpose, we had adopted an extra trigger mode to allow the heavy particles. The charge of particles could be measured from the track width in scintillating fibers since it is related to the ionization loss that is proportional to Z^2. The charge resolution was determined as $0.4Z$ from the distribution of track widths in the region of $Z = 2$–26. Then, singly-charged particles could easily be separated from heavy particles. The events that satisfy the criterion in cut 3, therefore, should be mostly electrons or protons. For gamma rays, more elaborate analysis of the incident particle is necessary and is presented later.

If the shower core were located near the edge of S_3, the leakage of shower energy would become dominant, and the energy resolution would be worse. The "edge cut" in item 4 was applied to select the events for which shower energies were contained almost inside the detector.

6.2. *Electron Selection by the RE-cut*

The events surviving through the cuts from 1 to 3 should satisfy the criteria that were assumed in the simulation for electron selection using the *RE* distribution. We applied, therefore, the same analysis with the simulation on these events. Figure 13 presents the *RE* distribution of the observed events for BETS97. It had a distribution similar to that of the simulation in Figure 5 and to the distribution of the electron beams in Figure 11 in $RE > 0.7$. It is, therefore, very likely to select electrons by imposing the event cut over 0.7 (*RE*-cut), and the rejection power against protons by the *RE*-cut is nearly 20. Combined with that of the selection of "triggered events" described above, the total rejection power against protons is nearly 2000.

6.3. *Gamma-Ray Rejection*

Gamma rays could not be completely rejected by the instrument trigger since they often have backscattered charged particles at S_1 and have very similar features of shower development as electrons. The detection efficiency of gamma rays was estimated at 1.7% $\sim$ 9.8% for 10 $\sim$ 100 GeV by simulations. We have imposed gamma-ray rejection by using the positions of hits in the top layer of fibers.

TABLE 2

OBSERVED NUMBER FOR DATA ANALYSIS

Observed Object	BETS97	BETS98
Average residual atmosphere at level flight (g cm^{-2})	5.6	5.9
Live time of observation (s)	13,213	22,441
Number of triggered events[a]	54,835	135,668
Number of electron candidates[b]	497	852
Number of rejected events as gamma rays (>11.1 GeV)	21 (9)	44 (18)

[a] In this number, all of the events during flight, such as the calibration events, the events not at the level flight, are included.

[b] This number does not include the gamma-ray events in the next row.

TABLE 3

RAW NUMBER OF ELECTRON CANDIDATES AT THE TOP OF THE DETECTOR

Energy (GeV)	BETS97 (1997 June 2)	BETS98 (1998 May 24–25)	BETS97 + BETS98
11.1 – 13.9	86	129	215
13.9 – 17.5	60	102	162
17.5 – 21.9	27	57	84
21.9 – 30.7	36	40	76
30.7 – 43.2	19	33	52
43.2 – 60.7	9	16	25
60.7 – 85.3	4	6	10
85.3 – 119.8	0	4	4
Total	241	387	628

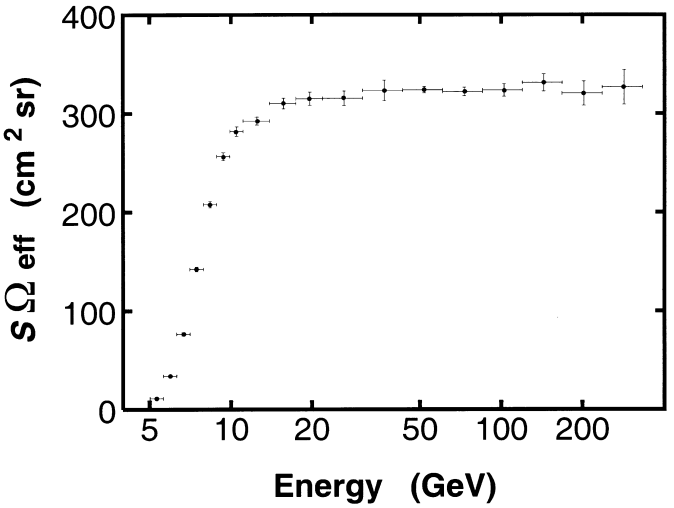

FIG. 14.—Energy dependence of the effective geometrical factors ($\epsilon\Omega A$) calculated by a Monte Carlo simulation.

Most electrons in the accelerator beams have more than one hit within 5 mm of the estimated shower axis. Gamma rays, therefore, could be identified by the presence of hits in the fibers separated from the shower axis more than 5 mm. The contamination of gamma rays could consequently be reduced to a negligible level.

6.4. *Energy Measurement*

About 1% of the recorded events remaining as electron candidates were submitted to the determination of energy by the pulse height at S_3 in a relation as presented in Figure 6. Effects of the inclination of the shower on the energy estimation were taken into account by employing the observed relations for different incident angles. In Table 2, some observed numbers used in the analysis are given for BETS97 and BETS98, and the raw numbers of electron candidates are tabulated in Table 3.

7. ABSOLUTE ENERGY SPECTRA

7.1. *Energy Spectra at the Top of Detector*

From the raw numbers, we evaluated the electron numbers (N_e) by correcting the proton contamination in the *RE*-cut. The number of electrons in $RE < 0.7$ ($N_{e/p}$) and that of protons in $RE \geq 0.7$ ($N_{p/e}$) were estimated from the *RE* distribution obtained by the Monte Carlo simulation. The number of electrons was given by $N_e - N_{p/e} + N_{e/p}$.

TABLE 4

ELECTRON FLUX AT THE TOP OF THE ATMOSPHERE

$E_{\rm ToA}$ (GeV)	$\bar{E}$ (GeV)	ΔE (GeV)	Intensity (m^{-2} s^{-1} sr^{-1} GeV^{-1})
12.5–15.7	13.9	3.15	$(7.20 \pm 0.49) \times 10^{-2}$
15.7–19.7	17.5	3.95	$(4.07 \pm 0.32) \times 10^{-2}$
19.7–24.7	21.9	5.00	$(1.66 \pm 0.18) \times 10^{-2}$
24.7–34.8	28.9	9.74	$(7.64 \pm 0.88) \times 10^{-3}$
34.8–48.8	40.6	13.7	$(3.62 \pm 0.50) \times 10^{-3}$
48.8–68.6	57.1	19.2	$(1.24 \pm 0.25) \times 10^{-3}$
68.6–96.4	80.2	27.0	$(3.5 \pm 1.1) \times 10^{-4}$
96.4–135.4.....	112.6	37.9	$(9.9 \pm 5.0) \times 10^{-5}$

This correction decreased the number of electrons by 11.5%.

The electron flux at the top of the detector was calculated by the effective geometrical factor (detection efficiency × solid angle × area; $\epsilon\Omega A$) and the observed live times. The geometrical factor was obtained for each energy bin from the simulations, as is shown in Figure 14. The geometrical factor is nearly constant, changing from ~280 cm^2 sr at 10 GeV to 320 cm^2 sr over 20 GeV. The increase of factor comes mainly from the detection efficiency in the instrument trigger. The live time in Table 2 was measured in the flights by counting the scalar clock cycles when the instrument was available for triggers. The fraction of live time to the total was 0.795 and 0.810 in BETS97 and BETS98, respectively.

Because of the resolution of the energy measurement, the energy spectrum should be changed in the flux since the "spillover" of events in adjacent energy bins causes a change of the flux in these bins. We have estimated this change by the assumption that the power-law spectral index, γ, and the energy resolution, σ, are constant in the applicable energy region. It is easily derived in such a case that the observed flux is higher than the real by a factor of $0.5(\gamma - 1)(\gamma - 2)\sigma^2$ without the change of γ. Then, the absolute intensities were decreased by a constant factor of 0.97 (for $\gamma = 3.0$; $\sigma = 0.17$) to reconstruct the absolute energy spectrum.

7.2. *Atmospheric Corrections*

In our previous report (Torii et al. 1999), the absolute energy spectrum at the top of the atmosphere (ToA) had been calculated by an attenuation factor of the primary electron energy spectrum at the observation level. The average attenuation factor, α, was 0.79 in BETS97 and of 0.78 in BETS98, respectively. However, in this paper, we have applied the method which considers the effect of transformation of the energy scale to ToA using the formula derived by J. Nishimura et al. (1980). The correction factor of energy, $\alpha^{(-1/(\gamma-1))}$, is given by 1.13 for both BETS97 and BETS98 in the case of $\gamma = 3.0$.

Table 4 presents the differential intensities of electrons at ToA in each energy interval. The effect of secondary electrons produced in the atmosphere by primary electrons and hadrons was neglected since the corrections should not exceed a level of 1% ~ 2%, as pointed out already in previous works (Nishimura et al. 1980; Barwick et al. 1998).

8. RESULTS AND DISCUSSIONS

Our results of the absolute differential intensities of electrons are plotted in Figure 15, multiplied by E^3 for clarity, for BETS97 and BETS98. The discrepancies between these two observations are considered to be not significant within the statistical errors. In Figure 16, we present the absolute intensities composed of BETS97 and BETS98 compared with the High-Energy Antimatter Telescope (HEAT) results (Barwick et al. 1998) that cover the same energy region. Our results are very consistent with HEAT, especially at the low-energy region where the event statistics are high. We can describe the BETS results by a single power-law spectrum; $0.199 \pm 0.015(E/10\ \text{GeV})^{-3.00 \pm 0.09}$ m^{-2} s^{-1} sr^{-1} GeV^{-1}.

However, the spectrum is not consistent with the CAPRICE results (Boezio et al. 2000). In fact, the difference is well outside the respective error bars. Although, as

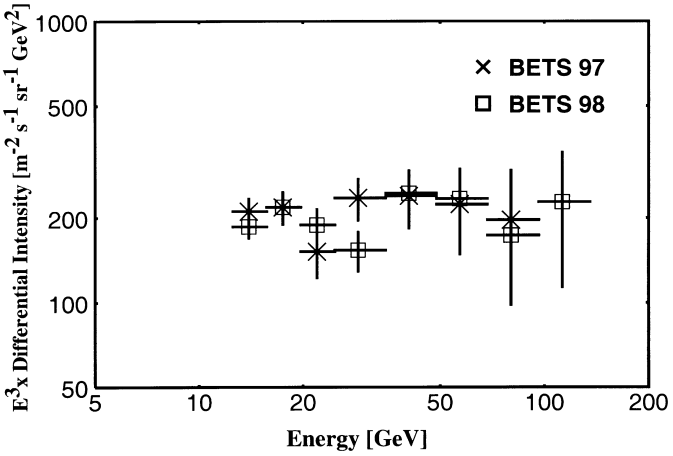

FIG. 15.—Electron differential energy spectra (scaled by E^3) at the top of the atmosphere observed in BETS97 and BETS98. The errors are statistical only.

pointed out by Boezio et al. (2000), a 20% systematic uncertainty in the energy estimation can explain the discrepancy, it is very unlikely for BETS since the uncertainty cannot exceed 5% from the accelerator beam tests at the same energies.

The solar activity was nearly minimum during the period of observations. The modulation parameter ϕ was estimated at 420 MV for BETS97 and at 630 MV for BETS98. This difference in the modulation parameters might give a change of the flux at 10 GeV by $\sim 10\%$ and have little effect above 20 GeV. A detailed study of modulation effects will be published elsewhere (Komori et al. 2000).

Some of the authors have calculated the electron spectrum by using a diffusion model (Nishimura et al. 1997). In that calculation, it was assumed that the SNRs, at a distance beyond 1 kpc and of an age older than 4×10^5 yr, distribute uniformly in the Galactic disk of radius 15 kpc and halo thickness 3 kpc. The explosion rate of supernovae was once per 30 yr, and the total energy of 1.5×10^{48} ergs above 1 GeV was released with a power-law index of 2.4 in the differential injection spectrum. The location of explosions was sampled randomly, and the propagation in the Galaxy was calculated by an analytical solution (Nishimura, Fujii, & Taira 1979) incorporating the energy dependence of energy-loss rate. The oldest age of an SNR was assumed to be 2×10^8 yr to estimate accurately the flux in as low an energy as 1 GeV. The flux from the nearby sources ($r < 1$ kpc and $t < 4 \times 10^5$ yr) was calculated by using the real objects observed by radio waves since the fluctuation effects on the energy spectrum must be correctly incorporated.

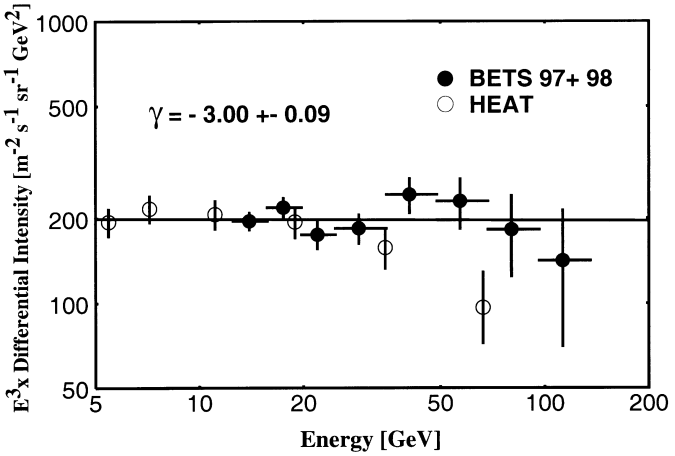

FIG. 16.—Observed absolute differential energy spectrum for electrons at the top of the atmosphere and the comparison with the HEAT results. The solid line shows a power-law fit to the BETS results; $0.199(E/10\ \mathrm{GeV})^{-3.00}\ \mathrm{m^{-2}\ s^{-1}\ sr^{-1}\ GeV^{-1}}$.

In Figure 17, we present the BETS results with previous measurements (Webber, Simpson, & Cane 1980; Tang 1984; Golden et al. 1984, 1994; Barwick et al. 1998; Kobayashi et al. 1999; Boezio et al. 2000) to compare with the calculation of two cases of diffusion coefficients. The coefficients have the same energy dependence, $E^{0.3}$, but the factor is different by a factor of 2. The larger factor gives the lower flux in the overall energy region. Our present results are very consistent with the model of $D = 2.0 \times 10^{28}$ $(E/1\ \mathrm{GeV})^{0.3}$ $\mathrm{cm^2\ s^{-1}}$, although it is difficult to answer which coefficient is preferable if we consider all of the present data.

Among several nearby sources listed in Nishimura et al. (1997), Monogem and Loop1 might have a significant contribution to the flux in the highest energy region. These fluxes are presented separately from the total flux of both the local sources and the distant sources for the lower diffusion coefficient.

It is known that the systematic discrepancy in the observations might result from two uncertainties. One is the absolute energy calibration as already mentioned, and the other is the absolute detection efficiency of the instrument. We believe that our results are very safe also from the uncertainty in the detection efficiency caused by the simple structure of the detector. The data statistics of our results, however, are insufficient to discuss the details of parameters in the calculation. We are planning to increase greatly our statistics by the long-duration ballooning of PPB (Polar Patrol Balloon) in Antarctica, which is scheduled in 2003 January.

The measurement of the energy spectrum in the TeV region is crucial to detect the nearby sources as understood from Figure 17. At present, in the energy region, only ECC could provide us the data, and the results are consistent with the presence of the nearby sources. Recently, the group has published new calculations in which the location of Vela is as near as 0.25 kpc by the latest estimation (Cha et al. 1999) instead of a distance of 0.5 kpc used in the present calculations. They claim that Vela is the most likely source for the electrons in TeV region (Kobayashi et al. 2001). If the electrons up to 10 TeV will be observed, we shall be able to identify the Vela existence as a high-energy electron source by observing the detailed spectral structure (Kobayashi et al. 2001) and the anisotropy in the arrival directions (Putsukin & Ormes 1995).

Moreover, the diffusion characteristics of electrons in the Galaxy can be studied in detail by using the knowledge of sources. We are preparing such an experiment at the international space station by developing an advanced BETS-type calorimeter (CALET) that is a combination of an imaging and a total absorption calorimeter (Torii et al. 2000b).

We express sincere thanks to the launch crew of the Sanriku Balloon Center in the Institute of Space and

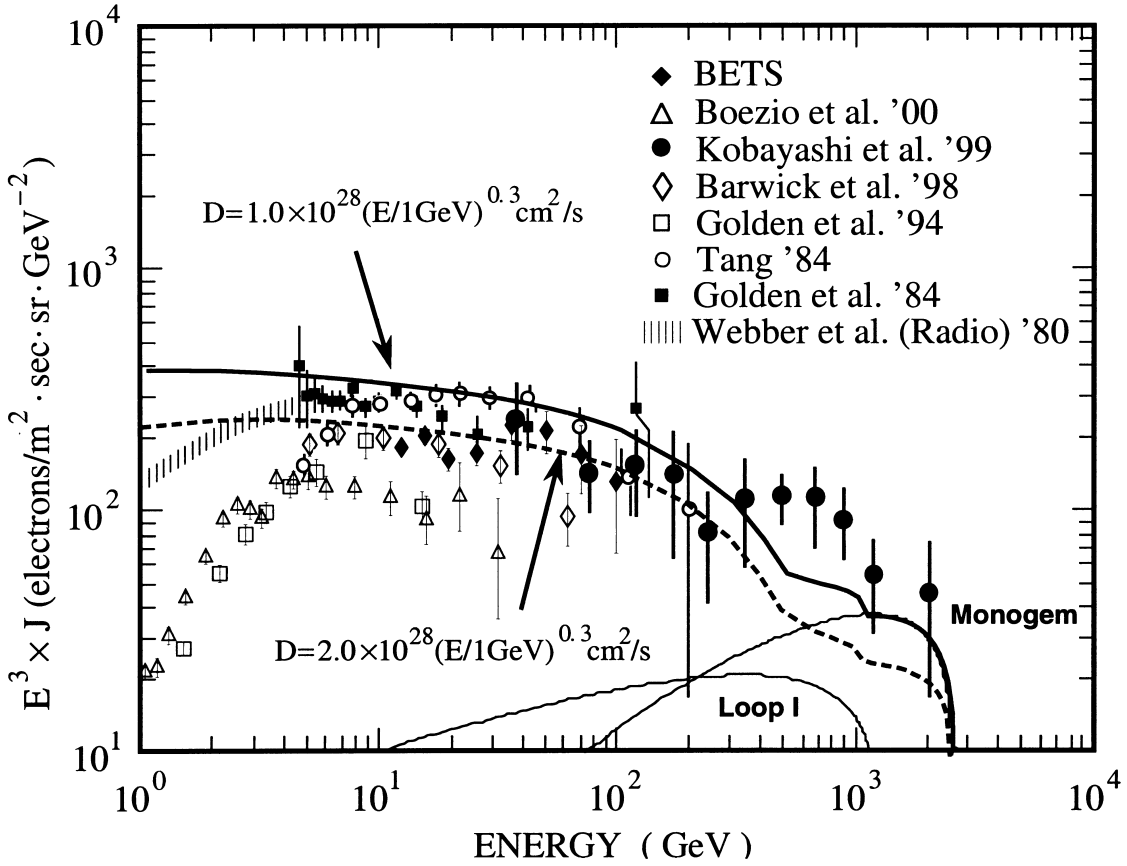

FIG. 17.—Absolute differential energy spectrum of electrons and the comparison with calculated results by a diffusion model assuming a power index of injection spectrum, 2.4. The solid line shows the results calculated by a diffusion coefficient of $D = 1.0 \times 10^{28}$ $(E/\mathrm{GeV})^{0.3}$ cm^2 s^{-1} with the individual contribution to the flux from the nearby sources (Loop1 and Monogem); the dashed line is for a coefficient larger by a factor of 2. In the latter, the flux from the nearby sources is not presented for the sake of simplicity.

Astronautical Science for the successful balloon flights. We also thank S. Suzuki, P. Picchi, and L. Periale for their support at CERN in the beam tests. We gratefully acknowledge assistance from L. Gatignon and the technical staffs at the X5 beam line of SPS at CERN. This work was supported by Grants-in-Aid for Scientific Research (A, B) and International Scientific Research, the Ministry of Education, Science, Sports and Culture.

REFERENCES

Atoyan, A. M., et al. 1995, Phys. Rev. D, 52, 3265
Barwick, S. W., et al. 1997, Nucl. Instrum. Methods Phys. Res. A, 400, 34
———. 1998, ApJ, 498, 779
Berezinskii, V. S., Bulanov, S., Dogiel, V., Ginzburg, V., & Ptuskin, V. 1990, Astrophysics of Cosmic Rays (Amsterdam: North-Holland)
Boezio, M., et al. 2000, ApJ, 532, 653
Buffington, A., Orth, C. D., & Smoot, G. F. 1975, ApJ, 199, 669
Cha, A. N., et al. 1999, ApJ, 515, L25
Daniel, R. R., & Stephens, S. A. 1965, Phys. Rev. Lett., 15, 769
Golden, R. L., et al. 1984, ApJ, 287, 622
———. 1994, ApJ, 436, 769
Kobayashi, T., Nishimura, J., Komori, Y., & Yoshida, K. 2001, Adv. Space Res., in press
Kobayashi, T., et al. 1999, Proc. 26th Int. Cosmic-Ray Conf. (Salt Lake City), 3, 62
Komori, Y., et al. 2000, J. Geophys. Res., submitted
Koyama, K., et al. 1995, Nature, 378, L255
Moskalenko, I. V., & Strong, A. W. 1998, ApJ, 493, 694
Müller, D., & Meyer, P. 1973, ApJ, 186, 841
Müller, D., & Tang, J. 1987, ApJ, 312, 183
Nishimura, J., et al. 1980, ApJ, 238, 394
———. 1997, Adv. Space Res., 19, 711
Nishimura, J., Fujii, M., & Taira, T. 1979, Proc. 16th Int. Cosmic-Ray Conf. (Kyoto), 1, 488
Pohl, M., & Esposito, J. A. 1998, ApJ, 507, 327
Prince, T. A. 1979, ApJ, 227, 676
Protheroe, R. J. 1982, ApJ, 254, 391
Putsukin, V. S., & Ormes, J. F. 1995, Proc. 24th Int. Cosmic-Ray Conf. (Roma), 3, 56
Tamura, T., et al. 2000, Adv. Space Res., 26, 1397
Tang, K. K. 1984, ApJ, 278, 881
Tanimori, T., et al. 1998, ApJ, 497, L25
Torii, S., et al. 1999, Proc. 26th Int. Cosmic-Ray Conf. (Salt Lake City), 3, 53
———. 2000a, Nucl. Instrum. Methods Phys. Res. A, 452, 81
———. 2000b, AIP Conf. Proc. 504, ed. M. S. El-Genk (New York: AIP), 187
Webber, W. R., Simpson, G. A., & Cane, H. V. 1980, ApJ, 236, 448